



Large bulk resistivity and surface quantum oscillations in the topological insulator $\text{Bi}_2\text{Te}_2\text{Se}$

Zhi Ren, A. A. Taskin, Satoshi Sasaki, Kouji Segawa, and Yoichi Ando*

Institute of Scientific and Industrial Research, Osaka University, Ibaraki, Osaka 567-0047, Japan

(Received 11 November 2010; published 9 December 2010)

Topological insulators are predicted to present interesting surface transport phenomena but their experimental studies have been hindered by a metallic bulk conduction that overwhelms the surface transport. We show that the topological insulator $\text{Bi}_2\text{Te}_2\text{Se}$ presents a high resistivity exceeding $1 \Omega \text{ cm}$ and a variable-range hopping behavior, and yet presents Shubnikov-de Haas oscillations coming from the topological surface state. Furthermore, we have been able to clarify both the bulk and surface transport channels, establishing a comprehensive understanding of the transport in this material. Our results demonstrate that $\text{Bi}_2\text{Te}_2\text{Se}$ is, to our knowledge, the best material to date for studying the surface quantum transport in a topological insulator.

DOI: [10.1103/PhysRevB.82.241306](https://doi.org/10.1103/PhysRevB.82.241306)

PACS number(s): 73.25.+i, 71.18.+y, 72.20.My, 73.20.At

The three-dimensional (3D) topological insulator (TI) is characterized by a nontrivial Z_2 topology^{1,2} of the bulk wave function and it represents a topological quantum state realized in a band insulator. In theory, 3D TIs are insulating in the bulk and unusual metallic surface states consisting of spin-filtered Dirac fermions give rise to interesting surface transport phenomena.^{3–5} In reality, however, TI samples available today are invariably conducting in the bulk and charge transport is always dominated by the bulk current.^{6–13} Therefore, to exploit the surface transport properties of topological insulators, it is crucial to achieve a bulk-insulating state in a TI material.

Among the recently discovered TIs, Bi_2Se_3 has been the most attractive because of its simple surface-state structure.³ Unfortunately, near-stoichiometric Bi_2Se_3 is always *n* type owing to a large amount of Se vacancies. An isostructural material Bi_2Te_3 can be grown as *p* type,¹⁰ but usually it is also highly metallic, most likely due to antisite defects which are promoted by close electronegativities of Bi and Te. Significant efforts have been made^{6–10} to achieve bulk insulating behavior in Bi_2Se_3 and Bi_2Te_3 ; however, while an increase in resistivity with decreasing temperature has been observed, so far the bulk remains to be essentially a metal and a clearly insulating temperature dependence, such as the variable-range hopping (VRH) behavior,¹⁴ has never been reported. For example, by growing a Bi_2Te_3 single crystal with a compositional gradient, it was possible to observe a resistivity upturn at low temperature and to measure the surface quantum transport,¹⁰ but the resistivity remained low ($<12 \text{ m}\Omega \text{ cm}$) in absolute terms and the surface contribution to the transport did not exceed $\sim 0.3\%$.¹⁰ The situation is essentially the same^{6–9} in Bi_2Se_3 .

Given this difficulty, searching for a TI material better suited for achieving the bulk insulating state is obviously important. In this Rapid Communication, we report that the TI material $\text{Bi}_2\text{Te}_2\text{Se}$, which has an ordered tetradymite structure¹⁵ [Fig. 1(a)] with the basic quintuple-layer unit of Te-Bi-Se-Bi-Te and was recently confirmed to have a topological surface state,¹⁶ has desirable characteristics for surface transport studies. We found that high-quality single crystals of ordered $\text{Bi}_2\text{Te}_2\text{Se}$ show a high resistivity exceeding $1 \Omega \text{ cm}$, together with a VRH behavior which is a hallmark of an insulator; yet, they present Shubnikov-de Haas

(SdH) oscillations which signify the two-dimensional (2D) surface state consistent with the topological one observed by the angle-resolved photoemission spectroscopy (ARPES).¹⁶

By examining the difference in the doping chemistry between Bi_2Se_3 and Bi_2Te_3 , one may understand that the ordered $\text{Bi}_2\text{Te}_2\text{Se}$ has reasons to be superior: (i) the formation of Se vacancies is expected to be suppressed because the Se trapped between two Bi atoms is less exposed to evaporation due to stronger chemical bonding with Bi in this position; (ii)

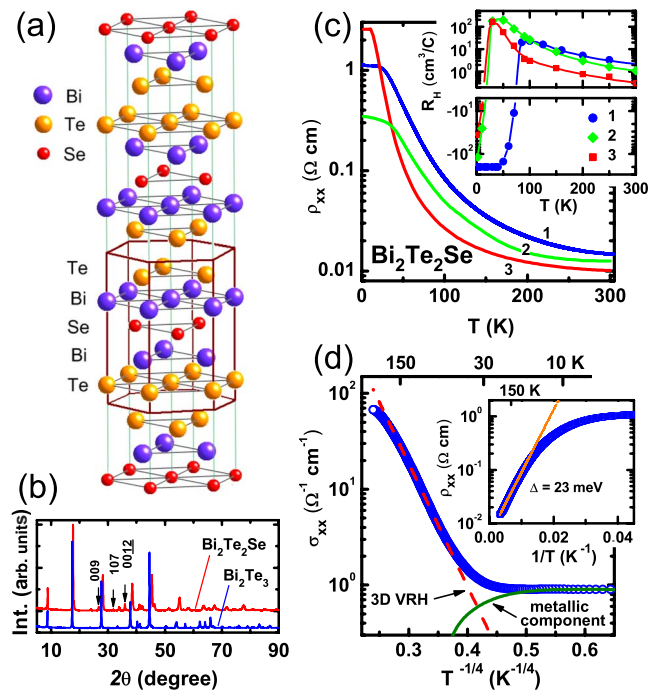


FIG. 1. (Color online) (a) Layered crystal structure of $\text{Bi}_2\text{Te}_2\text{Se}$ showing the ordering of Te and Se atoms. (b) Comparison of the x-ray powder-diffraction patterns of $\text{Bi}_2\text{Te}_2\text{Se}$ and Bi_2Te_3 . Arrows indicate the peaks characteristic of $\text{Bi}_2\text{Te}_2\text{Se}$. (c) Temperature dependence of ρ_{xx} for samples 1–3; inset shows $R_H(T)$ for the same samples. (d) Plot of the conductivity $\sigma_{xx}(=\rho_{xx}^{-1})$ vs $T^{-1/4}$ for sample 1. Dashed line is the fitting of the 3D VRH behavior $\sigma_{xx} \sim \exp[-(T/T_0)^{-1/4}]$ to the data; deviation from the fitting at low temperature, shown by solid line, signifies the parallel metallic conduction. Inset shows the Arrhenius plot of ρ_{xx} .

the formation of the antisite defects between Te and Bi is also expected to be suppressed because of preferable bonding between Se and Bi in contrast to Se-Te bonding; (iii) ordered nature minimizes the additional disorder that could be caused by Se/Te randomness. In this work, single crystals of $\text{Bi}_2\text{Te}_2\text{Se}$ were grown by melting high purity (6N) elements of Bi, Te, and Se with a molar ratio of 2:1.95:1.05 at 850 °C for 2 days in evacuated quartz tubes, followed by cooling to room temperature over 3 weeks. The ordering of the chalcogen layers in our $\text{Bi}_2\text{Te}_2\text{Se}$ single crystals is confirmed by the x-ray powder-diffraction patterns by comparing those from $\text{Bi}_2\text{Te}_2\text{Se}$ and Bi_2Te_3 as shown in Fig. 1(b), where the characteristic peaks, which are intensified in the ordered $\text{Bi}_2\text{Te}_2\text{Se}$ compound,¹⁵ are indicated by arrows. Note that the ordering does not cause a doubling nor a symmetry change in the unit cell.

For transport measurements, cleaved crystals were aligned using the x-ray Laue analysis and cut along the principal axes and the (111) surface was protected by depositing an alumina thin film after cleaning the surface by bias sputtering with Ar ions. Ohmic contacts were prepared by using room-temperature cured silver paste. The sample used for the SdH study was 0.51 mm wide and 0.26 mm thick, with the voltage contact distance of 0.86 mm. The resistivity ρ_{xx} and the Hall resistivity ρ_{yx} were measured simultaneously by a standard six-probe method by sweeping the magnetic field between ± 14 T, during which the temperature was stabilized to within ± 5 mK. The sweep rate was 0.3 T/min.

Figure 1(c) shows the temperature dependence of the resistivity ρ_{xx} and the Hall coefficient R_H for three samples of this ordered compound, obtained from two different batches. One can see that a high resistivity is reproducibly achieved at low temperature. We observe roughly two orders of magnitude increase in ρ_{xx} upon cooling from room temperature, which is an indication of an insulating behavior. We used sample 1 for the detailed measurements reported here. The Arrhenius plot [inset of Fig. 1(d)] of ρ_{xx} for this sample shows an activated temperature dependence in the range from 300 K down to ~ 150 K with an excitation energy Δ of about 23 meV. Below ~ 100 K, the transport is understood as a parallel circuit of an insulating component characterized by a 3D VRH behavior¹⁴ and a metallic component that saturates below 20 K [Fig. 1(d)].

The saturation of the resistivity at low temperature implies a finite metallic conductivity at $T=0$ K. To clarify the nature of this metallic state, we employed the SdH oscillations, whose angular dependence in tilted magnetic fields can provide the information about the size and the shape of the Fermi surface (FS) and, more importantly, about the dimensionality of the FS. In our $\text{Bi}_2\text{Te}_2\text{Se}$ crystals, we observed SdH oscillations in both ρ_{xx} and ρ_{yx} (the latter presenting more pronounced oscillations), and the two show essentially the same frequency with a phase shift of approximately π .¹⁷ Figure 2(a) shows the derivative of ρ_{yx} with respect to the magnetic field B plotted in $1/B_{\perp} \equiv 1/(B \cos \theta)$ coordinates, where θ is the angle between B_{\perp} and the C_3 axis as shown schematically in the bottom inset. Two important features can be readily recognized: First, $d\rho_{yx}/dB$ is periodic in the inverse magnetic field, indicating the existence of a well-defined FS. Second, oscillations depend solely on B_{\perp} , imply-

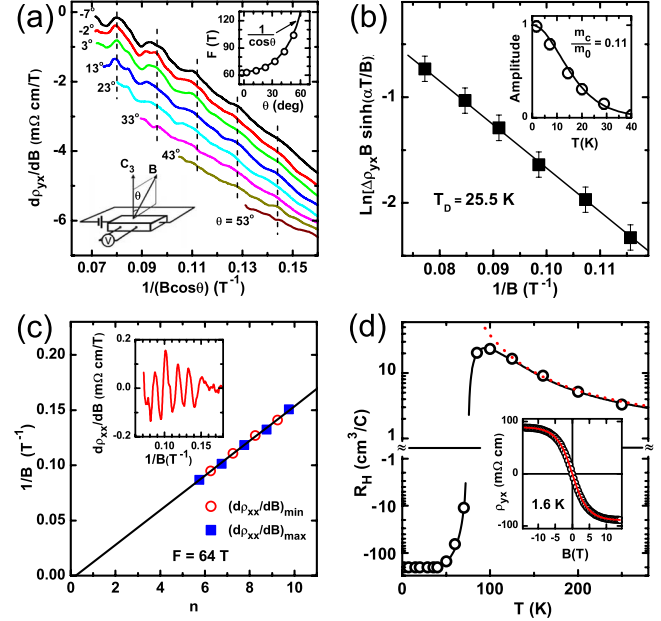


FIG. 2. (Color online) (a) $d\rho_{yx}/dB$ vs $1/B_{\perp} [=1/(B \cos \theta)]$ in magnetic fields tilted from the C_3 axis at different angles θ , where all curves are shifted for clarity; lower inset shows the schematics of the experiment and the definition of θ . Equidistant dashed lines in the main panel emphasize that the positions of maxima for any θ depends only on B_{\perp} ; upper inset shows the $1/\cos \theta$ dependence of the oscillation frequency. Both point to the 2D FS. (b) Dingle plot for the oscillations in $\Delta\rho_{yx}$, which is obtained after subtracting a smooth background from ρ_{yx} , giving $T_D = 25.5$ K; inset shows the T dependence of the SdH amplitude for $\theta = 0^\circ$, yielding $m_c = 0.11 m_e$. (c) Landau-level fan diagram for oscillations in $d\rho_{xx}/dB$ measured at $T = 1.6$ K and $\theta = 0^\circ$. Inset shows $d\rho_{xx}/dB$ vs $1/B$ after subtracting a smooth background. Minima and maxima in $d\rho_{xx}/dB$ correspond to $n + \frac{1}{4}$ and $n + \frac{3}{4}$, respectively. The least-square fitting intersects the axis at $n = 0.22 \pm 0.12$. (d) Temperature dependence of the low-field R_H ; dotted line represents the activated behavior. Inset shows the $\rho_{yx}(B)$ curve at 1.6 K and its fittings with the two-band model.

ing a 2D character. Note that the oscillations quickly disappear with increasing θ (above $\sim 40^\circ$ they are hardly distinguishable) because the amplitude of the oscillations strongly depends on the magnetic field strength. The signature of a 2D FS can be also seen in the plot of the oscillation frequency vs θ , which shows the characteristic $1/\cos \theta$ dependence [upper inset of Fig. 2(a)].

The obtained frequency for $\theta \approx 0^\circ$ of 64 T, which is directly related to the Fermi-surface cross section A via the Onsager relation $F = (\hbar c / 2\pi e) A$, gives $k_F = 4.4 \times 10^6$ cm⁻¹, corresponding to the surface carrier density $N_s = k_F^2 / 4\pi = 1.5 \times 10^{12}$ cm⁻² for a spin-filtered surface state. It is important to notice that our measured k_F is too large if the oscillations come from the bulk: For example, the carrier concentration for a 3D ellipsoidal FS that might be consistent with our SdH data would be $\geq 1 \times 10^{19}$ cm⁻³, which is orders of magnitude larger than what we obtain from the Hall data described later.

Fitting the standard Lifshitz-Kosevich (LK) theory¹⁸ to the temperature dependence of the SdH amplitudes [inset of

Fig. 2(b)] gives the cyclotron mass $m_c=0.11m_e$, where m_e is the free electron mass. Assuming that the electrons are Dirac type, one obtains the Fermi velocity $v_F=\hbar k_F/m_c=4.6\times 10^7$ cm/s. This v_F is consistent with the ARPES data,¹⁶ affirming the Dirac-fermion assumption. The position of the surface Fermi level E_F^s measured from the Dirac point can be estimated from v_F and k_F to be 130 meV, suggesting that the observed surface carriers are electrons. Note that, despite the unusual dispersion, the use of Onsager relation and the LK theory for Dirac electrons are fully justified, as shown experimentally¹⁹ and theoretically²⁰ for graphene.

Once m_c is known, the Dingle analysis [shown in Fig. 2(b)] uncovers the scattering time τ through the Dingle temperature $T_D[=\hbar/(2\pi\tau k_B)]$; the slope of the linear fit to the data yields T_D of 25.5 K, which gives $\tau=4.8\times 10^{-14}$ s. Hence, one obtains the mean-free path on the surface $\ell_s^{\text{SdH}}=v_F\tau\approx 22$ nm and the surface mobility $\mu_s^{\text{SdH}}=(e\ell_s^{\text{SdH}})/(\hbar k_F)\approx 760$ cm²/V s. Note that both quantities are underestimated, because τ obtained from the SdH effect reflects scattering events in all directions, whereas in the transport properties the backward scattering, which is prohibited in topological insulators,³ plays the most important role.

In the SdH oscillations, the resistivity oscillates as $\Delta\rho_{xx}\sim\cos[2\pi(\frac{E}{B}+\frac{1}{2}+\beta)]$, where $2\pi\beta$ is the Berry phase.²¹ It is known²¹⁻²⁴ that the cyclotron orbit of an electron in a magnetic field acquires a Berry phase π if its energy dispersion is linear near the degenerate point (called Dirac point), whereas in ordinary metals $\beta=0$. Experimentally, the phase of the oscillations is inferred from the Landau-level fan diagram, which is shown in Fig. 2(c) for the oscillations in $d\rho_{xx}/dB$.²⁵ The values of $1/B$ corresponding to minima and maxima in $d\rho_{xx}/dB$ [shown in Fig. 2(c) inset] are plotted as a function of the Landau-level number n .²⁶ The least-square fit to the data shown in Fig. 2(c) gives a finite $\beta=0.22\pm 0.12$, although the limited range of our analysis makes it difficult to deduce a firm conclusion about the Berry phase; hence, we leave it up to future studies to clarify this issue. In other studies of TIs, the Berry phase has always been ambiguous,^{7,10,12} and this could be due to the Zeeman effect that is amplified in TIs because of a large g factor.⁷

To elucidate the bulk contribution to the transport properties, the Hall data are useful. As shown in Fig. 2(d), the low-field Hall coefficient R_H ($=\rho_{yx}/B$ near $B=0$ T) changes sign from positive to negative upon cooling, signifying the change in dominant charge carries from holes to electrons. At high temperature (≥ 150 K), the behavior of $R_H(T)$ is thermally activated; the dotted line is an Arrhenius-law fitting, which signifies the activation of holes with an effective activation energy $\Delta^*=33$ meV. This Δ^* is of the same order as we found for the resistivity [inset of Fig. 1(d)] and the small difference is attributed to the temperature dependence of the mobility. The prefactor of the activated behavior gives an estimate of the acceptor concentration $N_a\approx 9\times 10^{18}$ cm⁻³.²⁷

When we look at the magnetic field dependence of ρ_{yx} at 1.6 K, the low-field and high-field slopes are essentially different [inset of Fig. 2(d)]. The low-field R_H is -200 cm³/C, giving the effective carrier concentration of 3.1×10^{16} cm⁻³. As we know from SdH oscillations, the surface-electron concentration is 1.5×10^{12} cm⁻²,

corresponding to an effective 3D Hall coefficient of -5.4×10^4 cm³/C, which is much larger than the observed value. Therefore, surface electrons alone cannot account for the low-temperature R_H and there should be other charge carriers in the system. Their concentration and type can be inferred from the high-field slope of $\rho_{yx}(B)$, since the high-field limit of R_H is determined only by the number (and type) of carriers irrespective of their mobilities; in our data, the high-field slope is -26 cm³/C, which points to the existence of bulk electrons with the concentration n of 2.4×10^{17} cm⁻³ in addition to the surface electrons. This example demonstrates that estimations of the bulk carrier density based on the low-field R_H , though often done in TIs,⁶⁻⁸ can be too optimistic.

The above analysis indicates that at low temperature the surface electrons and bulk electrons are contributing in parallel. It turns out that the standard two-band model²⁸

$$\rho_{yx}=\frac{(R_s\rho_n^2+R_n\rho_s^2)B+R_sR_n(R_s+R_n)B^3}{(\rho_s+\rho_n)^2+(R_s+R_n)^2B^2}, \quad (1)$$

fits the whole $\rho_{yx}(B)$ curve very well [solid line in the inset of Fig. 2(d)]; here, R_n and ρ_n are the Hall coefficient and resistivity of the bulk electrons, $R_s=t/(eN_s)$ and $\rho_s=\rho_{\square}t$, with ρ_{\square} the surface sheet resistance and t the sample thickness. This fitting yields the surface mobility $\mu_s=1450$ cm²/V s and the bulk mobility $\mu_n=11$ cm²/V s, along with $N_s=1.5\times 10^{12}$ cm⁻² and $n=2.4\times 10^{17}$ cm⁻³. The obtained μ_s is about two times larger than the μ_s^{SdH} estimated from the SdH analysis [Fig. 2(b)]. This is expected for the topological surface state as we mentioned before. On the other hand, the bulk mobility μ_n of 11 cm²/V s is near the boundary between the band and hopping transport regimes,¹⁴ suggesting that the bulk electrons move in a very disordered potential. The fraction of the surface contribution in the total conductance at 1.6 K is calculated to be $\sim 6\%$, which is more than 20 times larger than that achieved in Bi₂Te₃ (Ref. 10) or in Bi₂Se₃ (Ref. 29).

From the detailed information we have gathered a comprehensive picture emerges for the bulk transport mechanism in Bi₂Te₂Se: taking into account the relatively large concentration (9×10^{18} cm⁻³) of acceptors, it is reasonable to assume that those acceptors form an impurity band (IB) within the energy gap of Bi₂Te₂Se; note that the IB is formed because the wave functions of the electrons bound to impurity sites overlap to form extended states, which are responsible for the finite n -type bulk conduction at zero temperature with $n=2.4\times 10^{17}$ cm⁻³. The chemical potential is pinned to this IB at low temperature and is obviously located within the bulk energy gap (Fig. 3).³⁰ Since the formation of the extended states in the IB is essentially a percolation process,³¹ both localized and extended electrons coexist in the IB (this can also be understood in terms of the ‘‘mobility edge’’¹⁴); therefore, as the temperature increases, hopping conduction of localized electrons can take place alongside the degenerate IB conduction, giving rise to the VRH channel seen in Fig. 1(d). At higher temperature, thermal activation of electrons from the bulk valence band to the acceptors creates holes in the valence band, leading to the p -type bulk conduction.

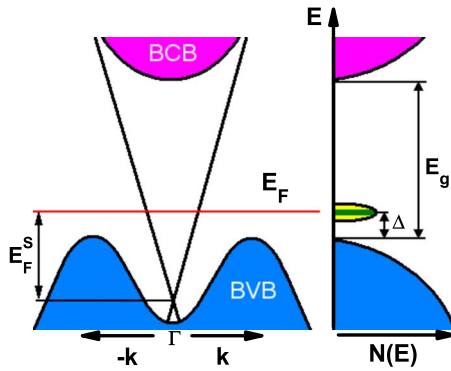


FIG. 3. (Color online) Schematic picture of the bulk and surface band structures (left), together with the energy diagram of the density of states of the bulk and impurity bands (right), where $E_F^s = 130$ meV, $\Delta \approx 30$ meV, and $E_g \approx 300$ meV. In the impurity band which is due to the acceptor levels and is located within the band gap, only the central part forms the extended states and the tails consist of localized states.

As for the alternative possibilities to explain the sign change in R_H , it is not likely that our sample is a mixture of electron-doped and hole-doped regions, because at low T the

$\rho_{yx}(B)$ behavior points to the existence of only one type of bulk carriers besides the surface carriers. Also, coexistence of a holelike 2D electron gas due to band bending is not likely because the Fourier transform of our SdH data show only one frequency.

In conclusion, we have shown that $\text{Bi}_2\text{Te}_2\text{Se}$ is, to our knowledge, the best material to date for studying the surface quantum transport in a TI. The surface contribution in the total conductance of our $\text{Bi}_2\text{Te}_2\text{Se}$ crystal is $\sim 6\%$, which is, to the best of our knowledge, the largest ever achieved in a TI. The bulk mobility of $11 \text{ cm}^2/\text{Vs}$ indicates that the IB conduction in our sample is at the verge of localization and not much further reduction in the number of acceptors would be needed to quench the degenerate bulk conduction. Once such crystals become available, they will allow us to study the plethora of topological quantum phenomena that have been predicted³⁻⁵ for this class of materials.

We thank L. Fu, M. Z. Hasan, N. P. Ong, and D. Vanderbilt for helpful discussions. This work was supported by JSPS (KAKENHI Grant No. 19674002), MEXT (Innovative Area “Topological Quantum Phenomena” KAKENHI Grant No. 22103004), and AFOSR (Grant No. AOARD 10-4103).

*y_ando@sanken.osaka-u.ac.jp

¹L. Fu and C. L. Kane, *Phys. Rev. B* **76**, 045302 (2007).

²J. E. Moore and L. Balents, *Phys. Rev. B* **75**, 121306(R) (2007).

³M. Z. Hasan and C. L. Kane, *Rev. Mod. Phys.* **82**, 3045 (2010).

⁴J. E. Moore, *Nature (London)* **464**, 194 (2010).

⁵X. Qi and S. Zhang, *arXiv:1008.2026* (unpublished).

⁶J. G. Checkelsky, Y. S. Hor, M.-H. Liu, D.-X. Qu, R. J. Cava, and N. P. Ong, *Phys. Rev. Lett.* **103**, 246601 (2009).

⁷J. G. Analytis *et al.*, *Nat. Phys.* **6**, 960 (2010).

⁸N. P. Butch, K. Kirshenbaum, P. Syers, A. B. Sushkov, G. S. Jenkins, H. D. Drew, and J. Paglione, *Phys. Rev. B* **81**, 241301(R) (2010).

⁹K. Eto, Z. Ren, A. A. Taskin, K. Segawa, and Y. Ando, *Phys. Rev. B* **81**, 195309 (2010).

¹⁰D. X. Qu *et al.*, *Science* **329**, 821 (2010).

¹¹A. A. Taskin and Y. Ando, *Phys. Rev. B* **80**, 085303 (2009).

¹²A. A. Taskin, K. Segawa, and Y. Ando, *Phys. Rev. B* **82**, 121302(R) (2010).

¹³H. Peng *et al.*, *Nature Mater.* **9**, 225 (2010).

¹⁴B. I. Shklovskii and A. L. Efros, *Electronic Properties of Doped Semiconductors* (Springer-Verlag, Berlin, 1984).

¹⁵O. B. Sokolov *et al.*, *J. Cryst. Growth* **262**, 442 (2004).

¹⁶S. Xu, L. Wray, Y. Xia, R. Shankar, A. Petersen, A. Fedorov, H. Lin, A. Bansil, Y. Hor, D. Grauer, R. Cava, and M. Hasan, *arXiv:1007.5111* (unpublished).

¹⁷The observed phase shift of $\sim \pi$ is at odds with the expected $\frac{\pi}{2}$ shift (Ref. 10). The reason for this unexpected observation is not clear at the moment.

¹⁸D. Shoenberg, *Magnetic Oscillations in Metals* (Cambridge University Press, Cambridge, 1984).

¹⁹K. S. Novoselov *et al.*, *Nature (London)* **438**, 197 (2005).

²⁰V. P. Gusynin and S. G. Sharapov, *Phys. Rev. B* **71**, 125124 (2005).

²¹Y. Zhang *et al.*, *Nature (London)* **438**, 201 (2005).

²²G. P. Mikitik and Yu. V. Sharlai, *Phys. Rev. Lett.* **82**, 2147 (1999).

²³D. Xiao, M. C. Chang, and Q. Niu, *Rev. Mod. Phys.* **82**, 1959 (2010).

²⁴T. Ando, T. Nakanishi, and R. Saito, *J. Phys. Soc. Jpn.* **67**, 2857 (1998).

²⁵Since the oscillations in ρ_{yx} present the unusual π phase shift compared to those in ρ_{xx} , the phase analysis of ρ_{yx} is not very meaningful and we concentrate on ρ_{xx} here.

²⁶Since $d\Delta\rho_{xx}/dB \sim 2\pi\frac{E}{B^2}\sin[2\pi(\frac{E}{B} + \frac{1}{2} + \beta)]$, we assign $n + \frac{1}{4}$ to the minima (and $n + \frac{3}{4}$ to the maxima) in $d\rho_{xx}/dB$.

²⁷In the extrinsic range, $R_H(T)$ is determined by Δ^* and N_a as $R_H^{-1} \approx e\sqrt{N_a N_V} \exp(-\Delta^*/k_B T)$, where $N_V = 2(2\pi m_p^* k_B T / \hbar^2)^{3/2}$ is the effective density of states of the valence band with m_p^* the effective density-of-state mass. m_p^* is not known for $\text{Bi}_2\text{Te}_2\text{Se}$, but if we take $m_p^* = 0.106m_e$ measured for Bi_2Te_3 (Ref. 32), $N_V = 5.2 \times 10^{18} \text{ cm}^{-3}$ at 300 K and N_a is estimated to be about $9 \times 10^{18} \text{ cm}^{-3}$.

²⁸N. W. Ashcroft and D. N. Mermin, *Solid State Physics* (Holt-Saunders, Holt-Saunders Japan, Tokyo, 1976), p. 240.

²⁹The surface contribution in Sb-doped Bi_2Se_3 estimated from the data in Ref. 7 for “sample $\Sigma 1$ ” is $\sim 0.1\%$.

³⁰The IB was not seen by ARPES (Ref. 16), which is probably because the density of the extended states is too thin. Given their low density, it is unlikely that they modify the surface state spectrum.

³¹J. C. Phillips, *Solid State Commun.* **47**, 191 (1983).

³²H. Köhler, *Phys. Status Solidi B* **74**, 591 (1976).